As per UGC guidelines an electronic bar code is provided to secure your paper

International Journal for Modern Trends in Science and Technology
Volume 12, Issue 07, pages 247-262.
ISSN: 2455-3778 online
Available online at: http://www.ijmtst.com/vol12issue06.html
DOI: https://doi.org/10.5281/zenodo.21535147

Power Quality Improvement and System Stability Enhancement in Grid-Connected PV-Battery System Using ANN Controlled DVR and Shunt Active Power Filter

G. Rupesh Kumar | J Nagaraju | Dr. K. Siva Kumar

Department of Electrical & Electronics Engineering, Sri Venkatesa Perumal College of Engineering and Technology, Puttur, Andhra Pradesh, India.

To Cite this Article
G. Rupesh Kumar, J Nagaraju & Dr. K. Siva Kumar (2026). Power Quality Improvement and System Stability Enhancement in Grid-Connected PV-Battery System Using ANN Controlled DVR and Shunt Active Power Filter. International Journal for Modern Trends in Science and Technology, 12(07), 247-262. https://doi.org/10.5281/zenodo.21535147

Article Info
Received: 18 June 2026; Revised: 18 July 2026; Accepted: 23 July 2026.

KEYWORDS

Artificial Neural Network (ANN), Battery Energy Storage System (BESS), Dynamic Voltage Restorer, Grid-Connected PV System, Harmonic Compensation, Power Quality Improvement, Shunt Active Power Filter, Voltage Sag and Swell.

ABSTRACT

This paper presents an enhanced control strategy for improving power quality and system stability in a low-voltage grid-connected solar photovoltaic (PV) and battery energy storage system. In the proposed system, a Dynamic Voltage Restorer (DVR) is integrated at the grid side to mitigate power quality disturbances such as voltage sag and voltage swell, thereby ensuring reliable and continuous power supply to the connected load. The PV array is connected to the DC bus through a DC–DC boost converter for maximum power extraction, while the battery energy storage system supports bidirectional power flow for charging and discharging operations based on system demand. To achieve intelligent and adaptive control, an Artificial Neural Network (ANN) controller is employed for the DVR operation. The ANN controller accurately detects voltage disturbances and generates appropriate compensation signals in real time, resulting in faster dynamic response and improved disturbance rejection compared with conventional controllers. In addition, the proposed control strategy enhances voltage regulation, reduces harmonic distortion, improves power factor, and maintains DC bus stability under varying grid and load conditions. The complete system is modeled and analyzed using MATLAB Simulink. Simulation results demonstrate effective mitigation of voltage sag and swell, improved load voltage profile, enhanced system stability, and reduction of total harmonic distortion (THD) within the limits specified by the Institute of Electrical and Electronics Engineers IEEE-519 standard. The proposed method provides an efficient and reliable solution for renewable energy integrated smart grid applications.

1. INTRODUCTION

The increasing penetration of renewable energy resources and the rapid growth of electric power demand have accelerated the development of grid-connected photovoltaic (PV) systems integrated with battery energy storage systems (BESS) for sustainable power generation and improved energy management [1]. Among various renewable energy technologies, solar photovoltaic generation has emerged as one of the most promising alternatives to conventional fossil fuel-based power plants because of its environmental benefits, modular structure, and declining installation costs [2]. However, the intermittent nature of solar irradiance and continuously varying load conditions introduce significant operational challenges in maintaining voltage regulation, power quality, and overall system stability in low-voltage distribution networks [3]. Consequently, advanced control techniques and power conditioning devices have become essential to ensure reliable integration of renewable energy resources into modern smart grids [4]. Power quality has become one of the major concerns in contemporary electrical distribution systems due to the widespread utilization of nonlinear loads, power electronic converters, distributed generation units, and renewable energy sources [5]. These factors introduce various power quality disturbances, including voltage sag, voltage swell, harmonic distortion, voltage flicker, and reactive power imbalance, which adversely affect sensitive industrial, commercial, and residential equipment [6]. Poor power quality not only reduces system efficiency but also increases maintenance costs, shortens equipment lifetime, and may result in unexpected interruptions of critical electrical loads [7]. Therefore, maintaining acceptable voltage profiles and minimizing harmonic distortion have become primary objectives in grid-connected renewable energy systems [8]. Voltage sag and voltage swell are among the most frequently occurring power quality disturbances in modern distribution systems [9]. Voltage sag generally occurs because of short-circuit faults, transformer energization, motor starting, or sudden increases in load demand, whereas voltage swell may arise due to abrupt load removal, capacitor bank switching, or network configuration changes [10]. These disturbances can significantly degrade the performance of sensitive electronic equipment, industrial drives, communication systems, and renewable energy converters [11]. Consequently, effective voltage compensation techniques are required to maintain uninterrupted power supply and enhance system reliability [12]. Custom power devices have been extensively investigated as practical solutions for mitigating power quality disturbances in distribution networks [13]. Among these devices, the Dynamic Voltage Restorer (DVR) has attracted considerable attention because of its ability to compensate voltage sag and swell by injecting an appropriate series voltage into the distribution feeder [14]. The DVR operates as a series-connected power electronic compensator capable of restoring the load-side voltage to its nominal value without interrupting power delivery [15]. Owing to its fast response, compact structure, and high compensation capability, the DVR has become one of the most effective technologies for protecting sensitive loads against voltage disturbances in renewable energy integrated distribution systems [16]. In addition to voltage compensation, harmonic mitigation has become increasingly important due to the extensive use of power electronic converters in distributed generation systems [17]. Harmonic currents generated by nonlinear loads deteriorate voltage quality, increase power losses, reduce equipment efficiency, and may cause overheating of transformers and electrical machines [18]. To overcome these problems, Shunt Active Power Filters (SAPFs) have been widely adopted for harmonic current compensation and reactive power support [19]. The SAPF injects compensating currents equal in magnitude and opposite in phase to the harmonic components of the load current, thereby maintaining nearly sinusoidal source currents and improving the overall power factor [20]. The coordinated operation of DVR and SAPF provides simultaneous voltage compensation, harmonic mitigation, and reactive power compensation, resulting in significant enhancement of distribution system performance [21]. The integration of battery energy storage systems (BESS) with grid-connected PV systems further improves operational flexibility by balancing the mismatch between renewable power generation and load demand [22]. During periods of excess solar generation, the battery stores surplus energy, whereas during low irradiance conditions or sudden load variations, the stored energy is supplied to maintain continuous power delivery [23]. Consequently, battery energy storage contributes to DC-link voltage stabilization, peak load management, improved renewable energy utilization, and enhanced overall system reliability [24]. Although conventional proportional-integral (PI), proportional-resonant (PR), and fuzzy logic controllers have demonstrated satisfactory performance under steady-state operating conditions, their effectiveness may deteriorate under rapidly changing grid disturbances, nonlinear system dynamics, and parameter uncertainties [25]. Recently, Artificial Neural Network (ANN) based controllers have emerged as an intelligent control solution because of their powerful nonlinear approximation capability, adaptive learning characteristics, fast convergence, and superior disturbance rejection. ANN controllers can accurately identify system operating conditions and generate optimal compensation signals in real time without requiring an accurate mathematical model of the system. These characteristics enable faster voltage restoration, improved harmonic suppression, enhanced DC-link voltage regulation, and better dynamic stability compared with conventional control methods. Motivated by these advantages, this paper proposes an ANN-controlled Dynamic Voltage Restorer integrated with a Shunt Active Power Filter for improving power quality and system stability in a grid-connected PV-battery energy storage system. In the proposed configuration, the solar PV array is connected to the common DC bus through a DC–DC boost converter to maximize energy extraction, while the battery energy storage system supports bidirectional power flow to maintain power balance under varying operating conditions. The ANN controller continuously monitors the system voltage and generates appropriate control signals for the DVR to compensate voltage sag and voltage swell rapidly. Simultaneously, the SAPF suppresses harmonic currents, compensates reactive power, and improves source current quality. The coordinated operation of these devices enhances voltage regulation, maintains DC-link stability, improves power factor, and ensures reliable operation of the grid-connected renewable energy system under dynamic grid and load conditions. The effectiveness of the proposed control strategy is validated through detailed MATLAB/Simulink simulations under various operating scenarios. The simulation results demonstrate that the proposed ANN-controlled DVR and SAPF significantly improve voltage quality, mitigate harmonic distortion, enhance system stability, and provide reliable operation of the grid-connected PV-battery system, thereby offering an effective solution for future renewable energy-based smart grid applications.

II. SYSTEM CONFIGURATION

Fig. 1 shows the proposed grid-connected PV–battery energy storage system integrated with an ANN-controlled Dynamic Voltage Restorer (DVR) and a Shunt Active Power Filter (SAPF). The system consists of a three-phase utility grid, a solar PV array, a battery energy storage system (BESS), a common DC-link capacitor, a shunt-connected voltage source converter (VSC), a series-connected DVR, and a nonlinear load. The PV array is interfaced with the DC bus through a DC–DC boost converter employing the Perturb and Observe (P&O) maximum power point tracking (MPPT) algorithm, while the BESS is connected through a bidirectional DC–DC buck–boost converter to support charging, discharging, and DC-link voltage regulation. The SAPF is connected in parallel with the distribution feeder through an LCL filter to compensate current harmonics and reactive power, thereby improving the source current quality and power factor. The DVR is connected in series with the feeder through an injection transformer to mitigate voltage sag and voltage swell by injecting the required compensating voltage. An Artificial Neural Network (ANN) controller generates the switching pulses for the DVR voltage source inverter, providing fast and accurate voltage compensation. The coordinated operation of the DVR and SAPF significantly improves power quality, maintains DC-link stability, and reduces the total harmonic distortion (THD) to comply with the IEEE-519 standard.

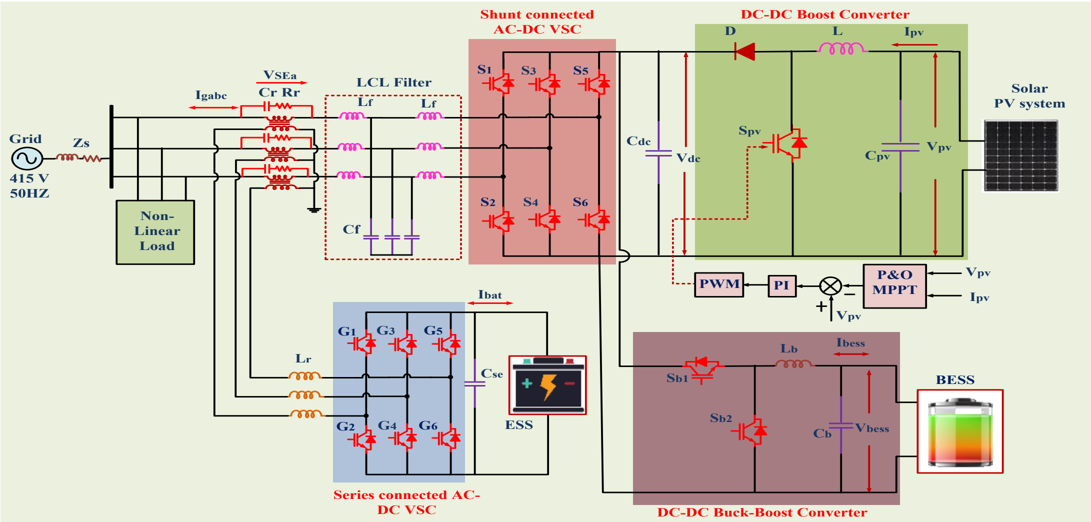

Fig. 1. Proposed system configuration of the grid-connected PV–BESS with ANN-controlled DVR and SAPF.

III. SOLAR PV SYSTEM CONFIGURATION

The proposed solar photovoltaic (PV) system consists of a PV array, a DC–DC boost converter, and a Perturb and Observe (P&O) maximum power point tracking (MPPT) controller, as shown in Fig. 2. The PV array converts solar energy into electrical energy, while the boost converter regulates the PV output voltage to the required DC-link voltage. The P&O MPPT algorithm continuously adjusts the converter duty cycle to ensure operation at the maximum power point under varying irradiance and temperature conditions.

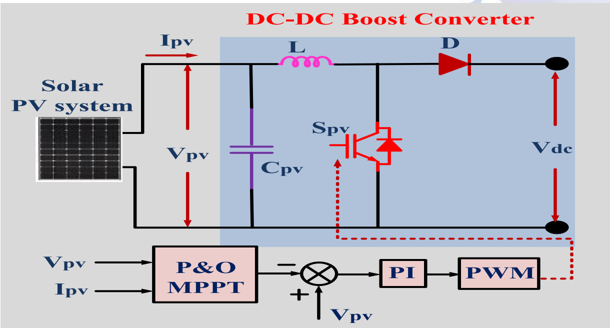

Fig. 2. Configuration of the solar PV system with DC–DC boost converter and P&O MPPT controller.

1) Equivalent Circuit of the Solar PV Cell

The electrical behavior of the solar PV cell is represented using the single-diode equivalent circuit, which consists of a photocurrent source, a diode, a series resistance, and a shunt resistance, as illustrated in Fig. 3.

The photocurrent generated by solar irradiation is expressed as

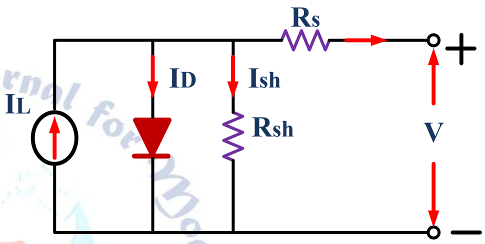

Fig. 3 equivalent model of PV solar.

$$I_{ph} = \left(I_{sc} + K_i\left(T - T_{ref}\right)\right)\frac{G}{G_{ref}} \quad (1)$$

where

- Isc = short-circuit current (A)
- Ki = temperature coefficient of current (A/K)
- T = operating temperature (K)
- Tref = reference temperature
- G = solar irradiance (W/m²)
- Gref =1000 W/m²

The diode current is

$$I_D = I_o\left[\exp\left(\frac{q\left(V_{pv}+I_{pv}R_S\right)}{nkT}\right) - 1\right] \quad (2)$$

where

- Io = reverse saturation current
- q = electron charge
- k = Boltzmann constant
- n = diode ideality factor
- Rs = series resistance

The shunt current is

$$I_{sh} = \frac{V_{pv}+I_{pv}R_S}{R_{sh}} \quad (3)$$

where Rsh is the shunt resistance.

Hence, the PV output current is

$$I_{pv} = I_{ph} - I_D - I_{sh}$$

Substituting (2) and (3),

$$I_{pv} = I_{ph} - I_o\left[\exp\left(\frac{q(V_{pv}+I_{pv}R_S)}{nkT}\right) - 1\right] - \frac{V_{pv}+I_{pv}R_S}{R_{sh}} \quad (4)$$

The output power of the PV array is

$$P_{pv} = V_{pv}I_{Pv} \quad (5)$$

2) DC–DC Boost Converter

Since the PV voltage varies continuously with environmental conditions, a boost converter is employed to increase the voltage to the desired DC-link level as shown in Fig.2.

The output voltage is

$$V_{dc} = \frac{V_{pv}}{1-D} \quad (6)$$

where

- D = duty cycle

The inductor voltage equation is

$$L\frac{di_L}{dt} = V_{pv} - (1-D)V_{dc} \quad (7)$$

The capacitor equation is

$$C\frac{dV_{dc}}{dt} = (1-D)i_L - I_{dc} \quad (8)$$

The state-space model is

$$\frac{d}{dt}\begin{bmatrix} i_L \\ V_{dc} \end{bmatrix} = \begin{bmatrix} 0 & \frac{1-D}{L} \\ \frac{1-D}{C} & 0 \end{bmatrix}\begin{bmatrix} i_L \\ V_{dc} \end{bmatrix} + \begin{bmatrix} \frac{1}{L} \\ 0 \end{bmatrix}V_{pv} + \begin{bmatrix} 0 \\ -\frac{1}{C} \end{bmatrix}I_{dc} \quad (9)$$

3) P&O MPPT Algorithm

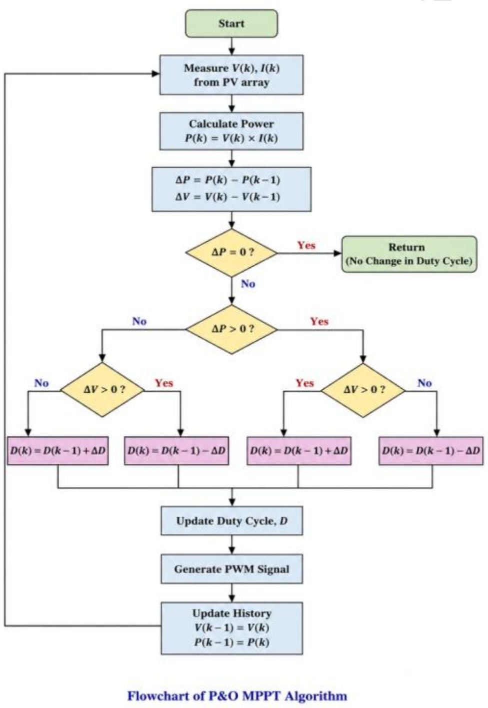

Fig. 4. Flowchart of the Perturb and Observe (P&O) Maximum Power Point Tracking (MPPT) algorithm.

The instantaneous PV power is

$$P(k) = V(k)I(k) \quad (10)$$

Power variation

$$\Delta P = P(k) - P(k-1) \quad (11)$$

Voltage variation

$$\Delta V = V(k) - V(k-1) \quad (12)$$

The MPPT decision rule is

$$\begin{cases} \Delta P > 0, & \Delta V > 0 \rightarrow D = D + \Delta D \\ \Delta P > 0, & \Delta V < 0 \rightarrow D = D - \Delta D \\ \Delta P < 0, & \Delta V > 0 \rightarrow D = D - \Delta D \\ \Delta P < 0, & \Delta V < 0 \rightarrow D = D + \Delta D \end{cases} \quad (13)$$

The voltage error is

$$e(t) = V_{ref} - V_{pv} \quad (14)$$

The PI controller is

$$u(t) = K_p e(t) + k_i \int e(t)\,dt \quad (15)$$

The PWM duty ratio is

$$D = f(u) \quad (16)$$

Thus, the boost converter continuously adjusts the switching duty cycle to operate the PV array at its maximum power point while maintaining a regulated DC-link voltage.

IV. MODELING AND DESIGN OF THE LITHIUM-ION BATTERY AND BIDIRECTIONAL DC–DC BUCK–BOOST CONVERTER

The proposed Battery Energy Storage System (BESS) consists of a lithium-ion battery interfaced with the common DC-link through a bidirectional DC–DC buck–boost converter, as illustrated in Fig. 5. The battery acts as an auxiliary energy source that stores excess photovoltaic energy during high generation periods and supplies energy to the DC bus whenever the renewable generation becomes insufficient. Consequently, the BESS improves system reliability, enhances DC-link voltage regulation, and enables continuous power delivery under varying operating conditions. Lithium-ion batteries are widely employed in renewable energy systems because of their high energy density, high charging efficiency, long cycle life, and low self-discharge characteristics. The battery terminal voltage depends on its open-circuit voltage, internal resistance, and charging or discharging current.

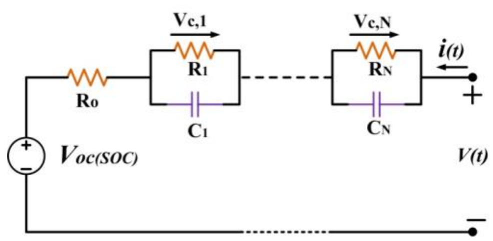

Fig.5: Equivalent circuit diagram of lithium ion EV battery

The battery voltage is expressed as

$$V_b = V_{oc} - I_b R_b \quad (17)$$

where

- Vb = battery terminal voltage (V),
- Voc = open-circuit voltage (V),
- Ib = battery current (A),
- Rb = internal resistance (Ω).

The battery power is given by

$$P_b = V_b I_b \quad (18)$$

where positive battery power represents the charging mode, while negative battery power corresponds to the discharging mode.

The battery state of charge (SOC) is determined as

$$SOC(\%) = SOC_0 + \frac{100}{Q_b} \int I_b dt \quad (19)$$

where

- SOC_0 = initial battery state of charge,
- Q_b = battery capacity (Ah).

A. Bidirectional DC–DC Buck–Boost Converter

A bidirectional DC–DC buck–boost converter is employed to regulate the bidirectional power transfer between the lithium-ion battery and the common DC-link. The converter operates in two modes according to the system power balance.

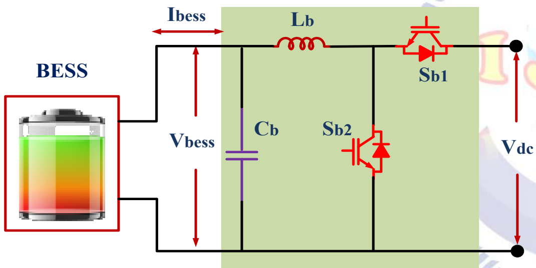

Fig. 6. Configuration of the Bidirectional DC–DC Buck–Boost Converter.

B. Buck Mode (Battery Charging)

During periods of surplus PV generation, the converter operates in the buck mode, where switch Sb1 is actively controlled while Sb2 remains OFF. The converter reduces the DC-link voltage to the required battery charging voltage, allowing energy to flow from the DC bus to the battery.

The voltage conversion ratio is

$$V_b = DV_{dc} \quad (20)$$

where

- D = duty cycle,
- Vdc = DC-link voltage.

The inductor current dynamics are

$$L_b \frac{dI_b}{dt} = DV_{dc} - V_b \quad (21)$$

B. Boost Mode (Battery Discharging)

When renewable generation is insufficient or the load demand increases, the converter operates in the **boost mode**, where switch Sb2 is controlled and the battery supplies power to the DC-link.

The boost converter voltage relationship is

$$V_{dc} = \frac{V_b}{1-D} \quad (22)$$

The inductor voltage equation is

$$L_b \frac{dI_b}{dt} = V_b - (1-D)V_{dc} \quad (23)$$

The DC-link capacitor dynamics are expressed as

$$C_b \frac{dV_{dc}}{dt} = (1-D)I_b - I_{dc} \quad (24)$$

where

- Lb = converter inductor,
- Cb = DC-link capacitor,
- I_{dc} = DC-link current.

The bidirectional DC–DC converter continuously regulates the power exchange between the lithium-ion battery and the common DC-link according to the system operating conditions. During high solar PV generation, the converter operates in the buck mode to charge the battery by transferring excess energy from the DC-link. Conversely, when the renewable power becomes insufficient or the load demand increases, the converter switches to the boost mode, allowing the battery to discharge and support the DC-link voltage. This bidirectional energy transfer improves renewable energy utilization, maintains DC-link voltage stability, reduces fluctuations caused by intermittent solar generation, and ensures reliable power supply to the connected load.

V. WORKING AND OPERATION OF THE BIDIRECTIONAL AC–DC CONVERTER WITH DYNAMIC VOLTAGE RESTORER

The proposed system employs a grid-connected bidirectional voltage source converter (VSC) integrated with a Dynamic Voltage Restorer (DVR) to improve power quality and enhance system stability under grid disturbances. The bidirectional AC–DC converter operates as a Shunt Active Power Filter (SAPF), whereas the DVR is connected in series with the distribution feeder to compensate voltage disturbances such as voltage sag and voltage swell. The coordinated operation of these converters ensures sinusoidal grid current, regulated DC-link voltage, reactive power compensation, harmonic mitigation, and uninterrupted load voltage under varying operating conditions.

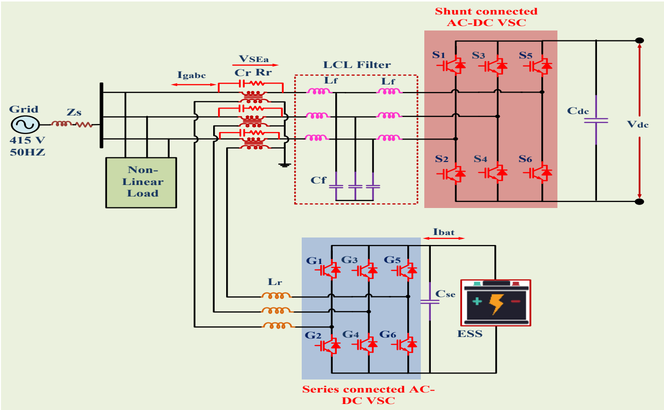

Fig. 7. Bidirectional AC–DC converter for harmonic mitigation and voltage compensation.

The shunt converter continuously exchanges active power between the DC-link and the utility grid while compensating harmonic currents generated by nonlinear loads. Simultaneously, the DVR injects a compensating voltage in series with the grid to restore the load voltage during voltage disturbances.

The three-phase grid voltages are expressed as

$$v_a = V_m \sin(\omega t) \quad (25)$$

$$v_b = V_m \sin\left(wt - \frac{2\pi}{3}\right) \quad (26)$$

$$v_c = V_m \sin\left(wt + \frac{2\pi}{3}\right) \quad (27)$$

The converter current dynamics are governed by

$$L_f \frac{di_g}{dt} = v_{inv} - v_g - R_f i_g \quad (28)$$

where

- Lf = filter inductance,
- Rf = filter resistance,
- vinv = converter output voltage,
- vg = grid voltage,
- ig = grid current.

The DC-link capacitor maintains a constant voltage and is represented by

$$C_{dc} \frac{dV_{dc}}{dt} = I_{dc} - I_{inv} \quad (29)$$

where

- Cdc = DC-link capacitor,
- Vdc = DC-link voltage,
- Idc = DC-link current,
- Iinv = converter current.

The instantaneous active and reactive powers are calculated as

$$P = \frac{3}{2}(v_d i_d + v_q i_q) \quad (30)$$

$$Q = \frac{3}{2}(v_q i_d + v_d i_q) \quad (31)$$

where

- vd,vq are the dq-axis voltages,
- id,iq are the dq-axis currents.

VI. DESIGN AND CONTROL OF SHUNT ACTIVE POWER FILTER (SAPF)

The proposed control strategy is developed for the Shunt Active Power Filter (SAPF) to achieve multifunctional compensation of nonlinear and unbalanced loads connected to the distribution network. The controller performs harmonic current compensation, reactive power compensation, load balancing, source current shaping, and DC-link voltage regulation simultaneously as shown in Fig.8. The reference currents are generated in the synchronous reference frame using the estimated fundamental load voltages and the available DC-link power.

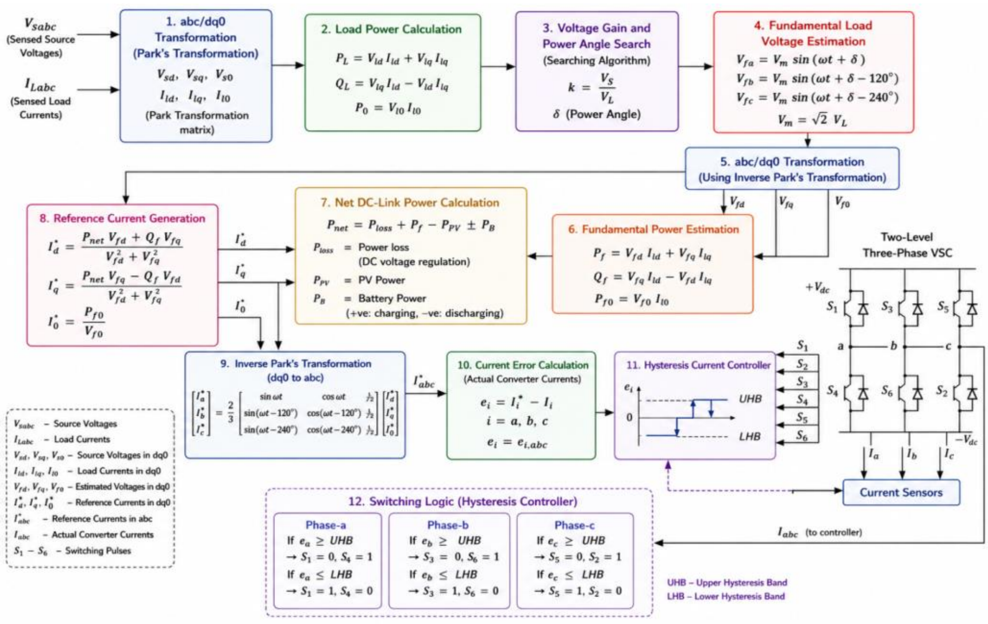

Fig.8 Control Algorithm of the Shunt Active Power Filter (SAPF)

A. Extraction of Fundamental Load Voltages

The three-phase source voltages and load currents are transformed into the synchronous rotating reference frame using the Park transformation.

$$\begin{bmatrix} V_d \\ V_q \\ V_0 \end{bmatrix} = \frac{2}{3}[T]\begin{bmatrix} V_a \\ V_b \\ V_c \end{bmatrix} \quad (32)$$

Where

$$[T] = \begin{bmatrix} \sin\omega t & \sin(\omega t - 120°) & \sin(\omega t - 240°) \\ \cos\omega t & \cos(\omega t - 120^0) & \cos(\omega t - 240^0) \\ 0.5 & 0.5 & 0.5 \end{bmatrix} \quad (33)$$

Similarly,

$$\begin{bmatrix} I_d \\ I_q \\ I_0 \end{bmatrix} = \frac{2}{3}[T]\begin{bmatrix} I_a \\ I_b \\ I_c \end{bmatrix} \quad (34)$$

The dq components represent the fundamental positive-sequence quantities, while the zero-sequence component represents the neutral current.

B. Estimation of Load Power

The active, reactive, and zero-sequence powers are calculated in the synchronous reference frame as

$$p_L = V_d I_d + V_q I_q \quad (35)$$

$$Q_L = V_q I_d - V_d I_q \quad (36)$$

$$P_0 = V_0 I_0 \quad (37)$$

These quantities represent the instantaneous power demanded by the nonlinear load.

C. Optimum Power Angle Estimation

The converter operating point is determined using the voltage gain

$$k = \frac{V_S}{V_L} \quad (38)$$

where

- VS = Source voltage
- VL = Load voltage

The optimum power angle (δ) is selected through the searching algorithm to maximize converter utilization while maintaining DC-link voltage regulation.

The estimated fundamental load voltages become

$$V_{fa} = V_m \sin(\omega t + \delta) \quad (39)$$

$$V_{fb} = V_m \sin(\omega t + \delta - 120^o) \quad (40)$$

$$V_{fc} = V_m \sin(\omega t + \delta - 240^o) \quad (41)$$

Where

$$V_m = \sqrt{2} V_L \quad (42)$$

D. Fundamental Power Estimation

The estimated voltages are transformed into dq coordinates.

The estimated active power is

$$P_f = V_{fd} I_d + V_{fq} I_q \quad (43)$$

The estimated reactive power is

$$Q_f = V_{fq} I_d - V_{fd} I_q \quad (44)$$

The zero-sequence power is

$$P_{f0} = V_{f0} I_0 \quad (45)$$

$$P_{f0} = V_{f0} I_0 \quad (46)$$

E. Net DC-Link Power Estimation

The net available DC-link power required for SAPF operation is

$$P_{net} = P_{loss} + P_f - P_{PV} \pm P_B \quad (47)$$

where

- P_{loss} = Converter losses
- P_{PV} = PV output power
- P_B = Battery power

Positive battery power indicates charging, while negative power represents discharging.

F. Reference Current Calculation

The d-axis reference current is

$$I_d^* = \frac{P_{net} V_{fd} + Q_f V_{fq}}{V_{fd}^2 + V_{fq}^2} \quad (48)$$

The q-axis reference current is

$$I_q^* = \frac{P_{net} V_{fq} + Q_f V_{fd}}{V_{fd}^2 + V_{fq}^2} \quad (49)$$

The zero-sequence reference current is

$$I_0^* = \frac{P_{f0}}{V_{f0}} \quad (50)$$

These equations determine the desired compensating currents required to regulate the DC-link voltage while providing harmonic elimination, reactive power compensation, and load balancing.

G. Inverse Park Transformation

The reference currents are transformed back into the abc frame using the inverse Park transformation

$$\begin{bmatrix} I_a^* \\ I_b^* \\ I_c^* \end{bmatrix} = [T^{-1}]\begin{bmatrix} I_d^* \\ I_q^* \\ I_0^* \end{bmatrix} \quad (51)$$

Where

$$[T^{-1}] = \begin{bmatrix} \sin\omega t & \cos\omega t & 0 \\ \sin(\omega t - 120°) & \cos(\omega t - 120°) & 0 \\ \sin(\omega t - 240°) & \cos(\omega t - 240°) & 0 \end{bmatrix} \quad (52)$$

H. Hysteresis Current Controller

The reference currents are compared with the measured SAPF currents.

The current error is

$$e_i = I_i^* - I_i \quad (53)$$

Where

$i = a, b, c$

The hysteresis controller maintains the compensating current within predefined upper and lower hysteresis bands.

For phase-a,

$I_a \geq I_a^* + UHB$ (54)

$S_1 = 0,\ S_4 = 1$

$I_a \leq I_a^* - LHB$

$S_1 = 1,\ S_4 = 0$

Similarly, for phase-b,

$I_b \geq I_b^* + UHB$ (55)

$S_3 = 0,\ S_6 = 1$

$I_b \leq I_b^* - LHB$

$S_3 = 1,\ S_6 = 0$

For phase-c,

$I_c \geq I_c^* + UHB$ (56)

$S_5 = 0,\ S_2 = 1$

$I_c \leq I_c^* - LHB$

$S_5 = 1, S_2 = 0$

The generated switching signals drive the two-level three-phase Shunt Active Power Filter (SAPF), ensuring accurate compensating current tracking, effective harmonic suppression, reactive power compensation, load current balancing, sinusoidal source current, unity power factor operation, and stable DC-link voltage under varying PV generation and battery operating conditions.

VII. DYNAMIC VOLTAGE RESTORER (DVR) CONTROLLER DESIGN

The proposed Dynamic Voltage Restorer (DVR) is employed to compensate voltage disturbances occurring at the point of common coupling (PCC) and to maintain a balanced sinusoidal voltage across the sensitive load as shown in Fig.9. The DVR is connected in series with the distribution feeder through a series injection transformer and is supplied by a common DC-link capacitor. The controller continuously monitors the source and load voltages, detects voltage sag and voltage swell, and generates appropriate switching pulses for the voltage source inverter (VSI) to inject the required compensating voltage.

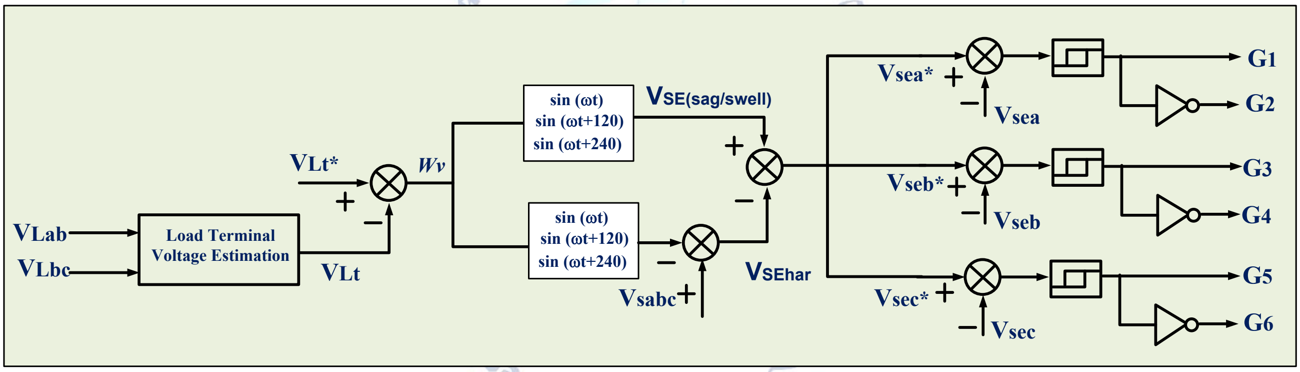

Fig. 9. Control strategy of the Dynamic Voltage Restorer (DVR)

Initially, the three-phase load terminal voltages VLa, VLb, and VLc are measured and processed by the Load Terminal Voltage Estimation block. The measured load voltage magnitude is obtained as

$$V_L = \sqrt{\frac{2}{3}(V_{La}^2 + V_{Lb}^2 + V_{Lc}^2)} \quad (57)$$

where VL denotes the fundamental load voltage magnitude.

The estimated load voltage is compared with the rated reference voltage to determine the voltage compensation requirement. The voltage error is expressed as

where

- VL∗ is the reference load voltage,
- VL is the measured load voltage.

The estimated voltage magnitude is then used to generate balanced sinusoidal reference voltages with the desired phase angle. The reference phase voltages are calculated as

$$V_{sa}^* = V_L \sin(\omega t + \delta) \quad (58)$$

$$V_{Sb}^* = V_L \sin\left(\omega t - \frac{2\pi}{3} + \delta\right) \quad (59)$$

$$V_{Sc}^* = V_L \sin\left(\omega t + \frac{2\pi}{3} + \delta\right) \quad (60)$$

where

- ω is the grid angular frequency,
- δ represents the phase compensation angle.

A. Voltage Sag and Swell Detection

The controller continuously compares the measured source voltage with the reference voltage. For voltage sag,

$V_s < V_{ref}$ (61)

For voltage swell,

$V_s > V_{ref}$ (62)

The compensating voltage injected by the DVR is determined as

$$V_{inj} = V_{ref} - V_s \quad (63)$$

Accordingly, the load voltage becomes

$$V_L = V_s + V_{inj} \quad (64)$$

During voltage sag, the injected voltage is in phase with the source voltage to restore the load voltage. Conversely, during voltage swell, the injected voltage is applied with opposite polarity to reduce the excessive source voltage.

B. Reference Voltage Generation

The compensating voltage references for each phase are obtained by subtracting the measured source voltages from the reference voltages,

$$V_{sea} = V_{sa}^* - V_{sa} \quad (65)$$

$$V_{seb} = V_{sb}^* - V_{sb} \quad (66)$$

$$V_{sec} = V_{sc}^* - V_{sc} \quad (67)$$

where

- Vsa, Vsb, and Vsc are the measured source voltages.

These error voltages represent the voltage that must be injected by the DVR through the series transformer.

C. Pulse Generation

The reference injected voltages are compared with the measured inverter output voltages to generate the switching error,

$$e_{sa} = V_{sea}^* - V_{sea} \quad (68)$$

$$e_{sb} = V_{seb}^* - V_{seb} \quad (69)$$

$$e_{sc} = V_{sec}^* - V_{sec} \quad (70)$$

The voltage errors are processed using a Pulse Width Modulation (PWM) controller to produce the switching signals for the voltage source inverter. The PWM switching logic is expressed as

$$S = \begin{cases} 1, & V_{ref} > V_{carrier} \\ 0, & V_{ref} < V_{carrier} \end{cases} \quad (71)$$

where

- V_{ref} is the reference modulation signal,
- $V_{carrier}$ is the triangular carrier waveform.

The generated gate pulses control the six inverter switches (G1–G6), enabling the VSI to synthesize the required compensating voltage and inject it into the distribution feeder through the series transformer. During normal operating conditions, the measured load voltage is equal to the reference voltage, and the DVR injects negligible voltage into the system. When voltage sag occurs, the controller detects the reduction in source voltage, computes the required compensating voltage, and commands the voltage source inverter to inject a series voltage that restores the load voltage to its nominal value. Similarly, during voltage swell, the controller generates an opposing compensating voltage to suppress the excessive grid voltage before it reaches the sensitive load. The continuous feedback of the measured voltages ensures fast dynamic response, accurate voltage compensation, and stable operation under varying grid conditions. Consequently, the proposed DVR controller effectively mitigates voltage sag and voltage swell, maintains sinusoidal load voltage, improves power quality, and enhances the reliability of the grid-connected PV-battery energy storage system.

VIII. ANN-BASED DC-LINK VOLTAGE REGULATION FOR THE SHUNT ACTIVE POWER FILTER

The proposed Artificial Neural Network (ANN) controller regulates the DC-link voltage of the Shunt Active Power Filter (SAPF) by replacing the conventional PI controller. The controller continuously monitors the DC-link voltage and estimates the active power required to compensate converter losses and maintain the DC-link voltage at its reference value. The ANN receives the DC-link voltage error and its rate of change as inputs and generates the active power component used for reference current generation as shown in Fig.10.

1) DC-Link Voltage Error

The reference DC-link voltage is compared with the measured DC-link voltage to produce the voltage error

$$e(k) = V_{dc}^* - V_{dc} \quad (72)$$

where

- V_{dc}^* = reference DC-link voltage
- V_{dc} = measured DC-link voltage

The change in voltage error is

$$\Delta e(k) = e(k) - e(k-1) \quad (73)$$

The ANN input vector is therefore

$$x = \begin{bmatrix} e(k) \\ \Delta e(k) \end{bmatrix} \quad (74)$$

2) Hidden Layer Processing

Each hidden neuron calculates the weighted sum of the inputs

$$Net_j = \sum_{i=1}^{n} w_{ij} x_i + b_j \quad (75)$$

where

- w_{ij} = input weight
- b_j = hidden layer bias

The neuron output is obtained using the tangent sigmoid activation function

$$H_j = f(Net_j) \tag{76}$$

Where

$$f(x) = \frac{2}{1+e^{-2x}} - 1 \tag{77}$$

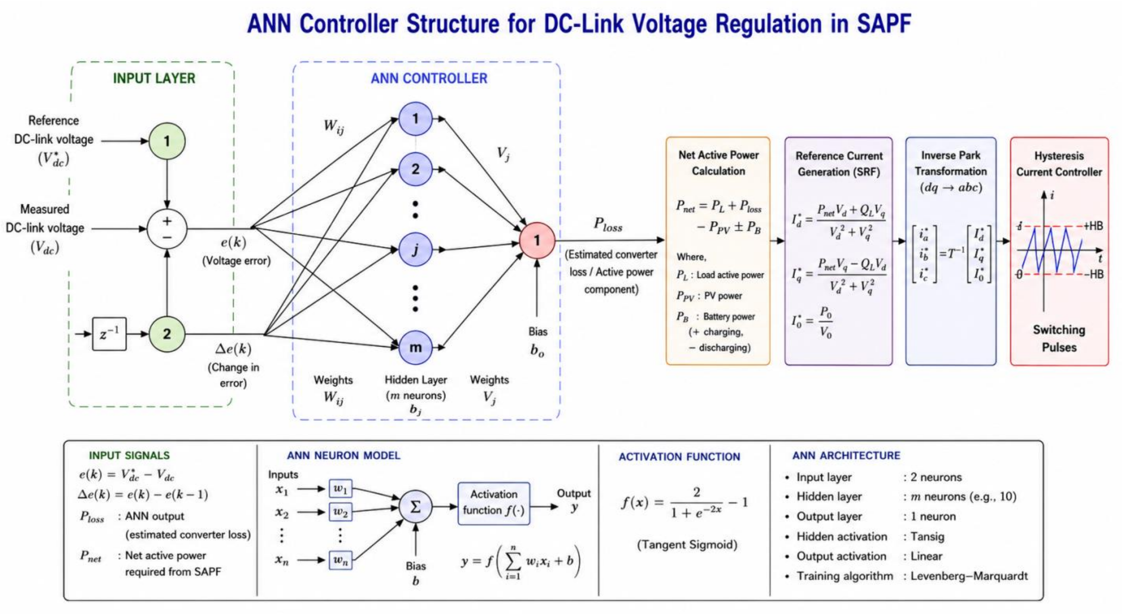

Fig. 10. ANN-Based Control Structure for the Shunt Active Power Filter.

3) Output Layer

The output neuron computes

$$Y = \sum_{j=1}^{m} V_j H_j + b_o \tag{78}$$

where

- Vj = hidden layer weight
- bo = output bias

The ANN output represents the converter active power required for DC-link voltage regulation,

$$P_{loss} = y \tag{79}$$

4) ANN Weight Update

The ANN weights are updated using the back propagation learning algorithm

$$w_{ij}(k+1) = w_{ij}(k) + \eta \delta_j x_i \tag{80}$$

The output error is

$$\delta = T - Y \tag{81}$$

where

- T = desired output
- Y = ANN output
- η = learning rate

The performance index is defined by the mean square error

$$MSE = \frac{1}{N} \sum_{i=1}^{N} (T_i - y_i)^2 \tag{82}$$

IX. SIMULATION RESULTS AND DISCUSSION

A. Grid-Connected Bidirectional AC–DC Voltage Source Converter Operating as a Shunt Active Power Filter

The performance of the proposed grid-connected bidirectional AC–DC voltage source converter (VSC) operating as a Shunt Active Power Filter (SAPF) is evaluated under dynamic operating conditions. Fig. 11 (a)–(e) present the simulated waveforms of the grid voltage, grid current, load current, load voltage, and DC-link voltage. The grid voltage shown in Fig. 11(a) remains balanced and sinusoidal throughout the simulation with a peak value of approximately ±325 V at 50 Hz, indicating proper synchronization between the converter and the utility grid. As shown in Fig. 11 (b), the grid current exhibits an initial transient reaching nearly ±58 A during converter startup due to DC-link charging. After stabilization, the current magnitude gradually decreases from approximately ±35 A to ±28 A, ±20 A, and finally ±14 A as the operating conditions change. The source currents remain balanced and nearly sinusoidal, demonstrating effective harmonic compensation. The load current in Fig. 11 (c) remains balanced with a constant peak value of approximately ±23 A, while the load voltage in Fig. 11 (d) maintains a sinusoidal waveform with a peak value of nearly ±325 V, confirming stable power delivery to the load. The

DC-link voltage, shown in Fig. 11 (e), initially increases from about 480 V to 790 V before settling at approximately 700 V within 0.05 s. Small voltage variations of nearly 10–15 V occur during load changes; however, the controller rapidly restores the DC-link voltage to its reference value. The simulation results verify that the proposed SAPF-based bidirectional AC–DC converter effectively suppresses harmonic currents, maintains balanced grid currents and voltages, regulates the DC-link voltage, and ensures stable operation under varying operating conditions.

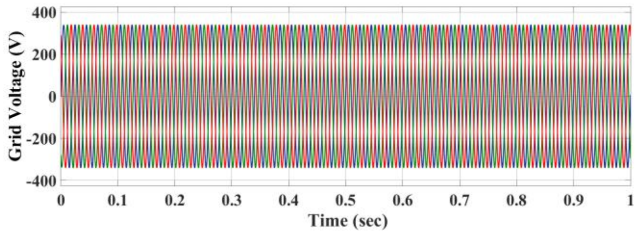

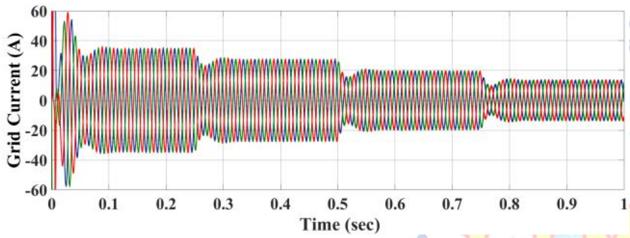

(a)

(b)

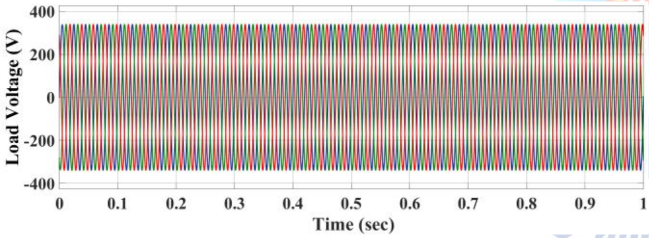

(c)

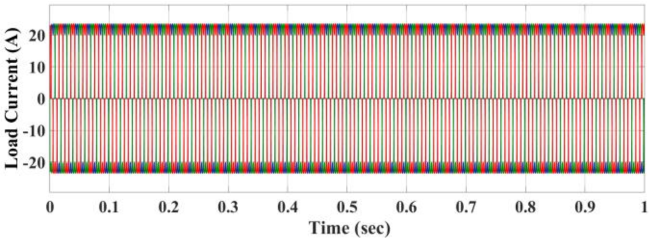

(d)

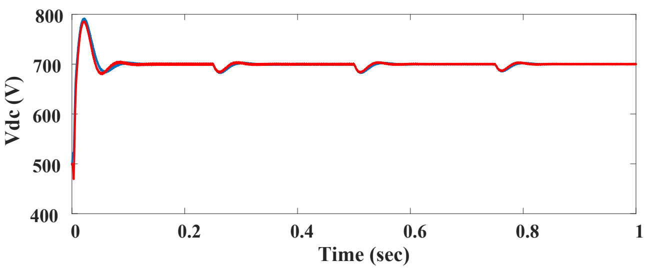

(e)

Fig. 11. Performance of the grid-connected bidirectional AC–DC voltage source converter operating as a shunt active power filter: (a) grid voltage, (b) grid current, (c) load current, (d) load voltage, and (e) DC-link voltage.

B. Performance Analysis of the Solar Photovoltaic System

The dynamic performance of the proposed solar PV system under varying irradiance conditions is illustrated in Fig. 12 (a)–(d). The solar irradiance is varied from 1000 W/m² to 750 W/m² at 0.25 s, reduced to 500 W/m² at 0.50 s, and finally decreased to 300 W/m² at 0.75 s, as shown in Fig. 12 (a). The corresponding PV output voltage, shown in Fig. 12 (b), remains nearly constant at approximately 305 V throughout the simulation despite the irradiance variations. Only small transient deviations are observed during irradiance transitions, demonstrating the effectiveness of the DC–DC boost converter and the P&O MPPT controller in maintaining stable PV voltage. As illustrated in Fig. 12 (c), the PV current changes according to the available solar irradiance. The current decreases from approximately 100 A at 1000 W/m² to 75 A, 50 A, and finally 30 A as the irradiance is reduced. This behavior confirms that the PV current is directly proportional to the incident solar radiation. The PV output power, shown in Fig. 12 (d), follows the irradiance profile by decreasing from approximately 30 kW to 22.5 kW, 15 kW, and finally 9 kW. The smooth transition between operating points indicates rapid maximum power tracking with negligible oscillations around the maximum power point. Overall, the simulation results demonstrate that the proposed P&O MPPT-controlled DC–DC boost converter effectively tracks the maximum power point under varying irradiance conditions while maintaining stable PV voltage and ensuring efficient power extraction.

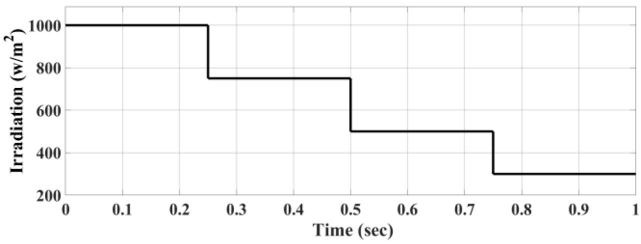

(a)

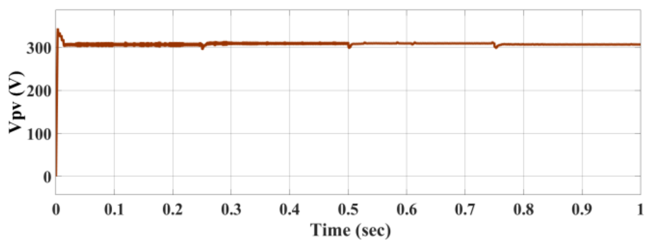

(b)

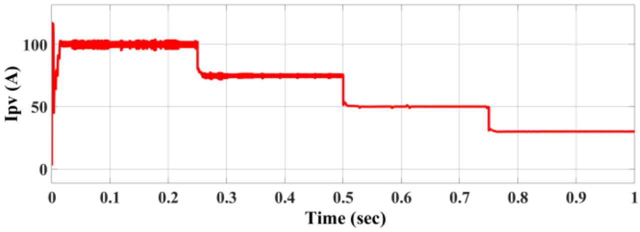

(c)

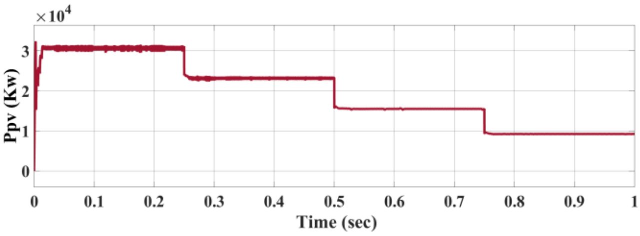

(d)

Fig. 12. Dynamic performance of the solar PV system: (a) solar irradiance, (b) PV output voltage, (c) PV output current, and (d) PV output power.

C. Performance Analysis of the Battery Energy Storage System

The dynamic performance of the Battery Energy Storage System (BESS) is presented in Fig. 13(a)–(d), which illustrates the battery terminal voltage, battery current, battery power, and battery state of charge (SOC) under varying operating conditions. The battery terminal voltage, shown in Fig. 13(a), remains nearly constant at approximately 325 V throughout the simulation with only a small transient during the initial startup period. This demonstrates the effectiveness of the bidirectional DC–DC converter in maintaining a stable battery voltage during charging operation. As illustrated in Fig. 13 (b), the battery current exhibits an initial transient reaching approximately 52 A, followed by a short discharging interval of about −15 A. After 0.25 s, the current gradually increases from approximately 10 A to 21 A at 0.50 s, and finally reaches nearly 31 A after 0.75 s, indicating controlled battery charging under different power demands. The corresponding battery power, shown in Fig. 13 (c), follows the current profile. Following an initial transient of approximately 17 kW, the battery briefly operates in the discharging mode at about −5 kW before switching to charging mode. The charging power subsequently increases to approximately 3.5 kW, 7.5 kW, and 10 kW as the charging current increases. The battery SOC, depicted in Fig. 13 (d), remains close to 63.81% throughout the simulation. A slight decrease is observed due to transient power exchange between the battery and the DC-link; however, the SOC variation is minimal, demonstrating effective battery energy management and stable converter operation. The simulation results confirm that the proposed bidirectional DC–DC converter provides smooth charging operation, maintains a stable battery voltage, regulates battery power effectively, and ensures reliable energy management under varying system conditions.

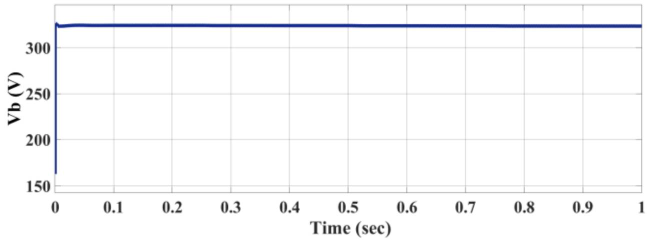

(a)

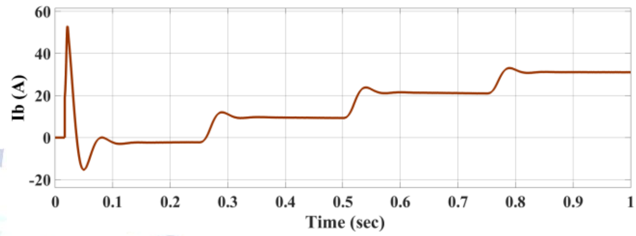

(b)

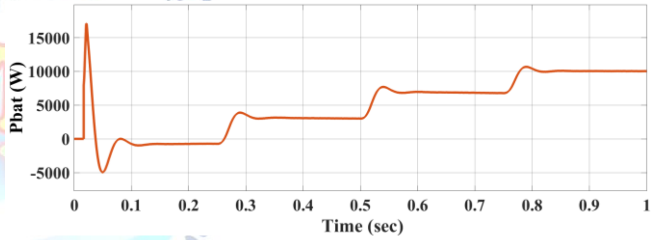

(c)

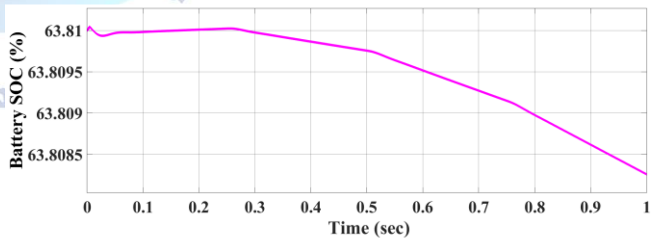

(d)

Fig. 13 . Dynamic performance of the battery energy storage system: (a) battery voltage, (b) battery current, (c) battery power, and (d) battery state of charge (SOC).

D. Performance Analysis of the Dynamic Voltage Restorer (DVR)

The performance of the proposed Dynamic Voltage Restorer (DVR) is evaluated under voltage sag and voltage swell conditions, as shown in Fig. 14 (a)–(c). The DVR is designed to compensate supply voltage disturbances by injecting an appropriate series voltage, thereby maintaining a balanced and sinusoidal load voltage. As illustrated in Fig. 14 (a), the grid voltage initially remains balanced with a peak value of approximately ±325 V. A voltage sag is introduced at 0.20 s, reducing the voltage to nearly ±250 V, while a voltage swell occurs at 0.60 s, increasing the voltage to approximately ±400 V. The grid voltage returns to its nominal value after 0.40 s and 0.80 s, respectively. The corresponding series injected voltage produced by the DVR is shown in Fig. 14 (b). During the voltage sag interval (0.20–0.40 s), the DVR injects a compensating voltage of approximately ±80 V in phase with the source voltage to restore the load voltage. Similarly, during the voltage swell interval (0.60–0.80 s), the DVR injects nearly ±65 V with opposite polarity to suppress the excessive supply voltage. Outside these disturbance intervals, the injected voltage remains close to 0 V, indicating normal operating conditions. The load voltage, presented in Fig. 14 (c), remains balanced and sinusoidal throughout the simulation with a peak value of approximately ±325 V despite the occurrence of voltage sag and voltage swell. This demonstrates the fast dynamic response and accurate compensation capability of the proposed DVR controller in maintaining a constant load voltage under varying grid disturbances. The simulation results confirm that the proposed DVR effectively mitigates voltage sag and voltage swell by injecting the required compensating voltage, thereby ensuring uninterrupted power supply, improved voltage regulation, and enhanced power quality for sensitive loads.

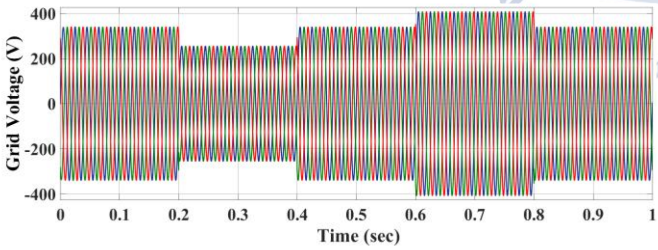

(a)

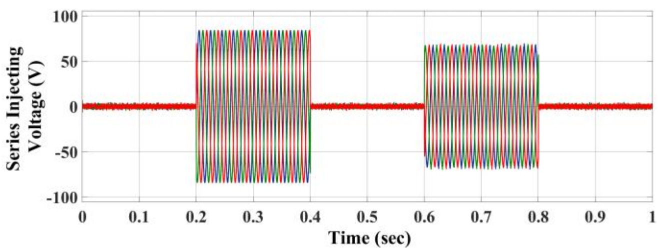

(b)

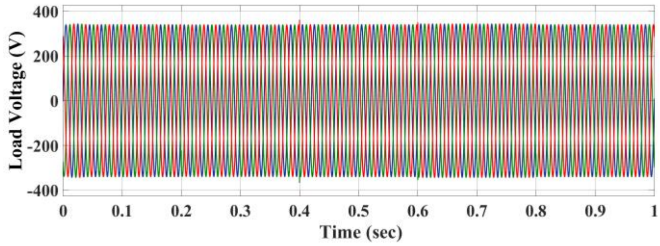

(c)

Fig. 14. Dynamic performance of the Dynamic Voltage Restorer (DVR): (a) grid voltage under voltage sag and swell conditions, (b) DVR series injected voltage, and (c) compensated load voltage.

E. Harmonic Analysis of Grid Current

The harmonic performance of the proposed controller is evaluated by comparing the Total Harmonic Distortion (THD) of the grid current using the conventional PI controller and the proposed Artificial Neural Network (ANN) controller, as shown in Fig. 15 (a) and Fig. 15 (b). As illustrated in Fig. 15 (a), the grid current controlled by the PI controller exhibits a THD of 5.00%, which is at the maximum permissible limit specified by the IEEE-519 standard. Although the PI controller maintains acceptable current quality, noticeable harmonic components are observed around the lower- and higher-order frequencies, indicating limited compensation capability under dynamic operating conditions. In contrast, the ANN controller, shown in Fig. 15 (b), significantly improves the harmonic performance by reducing the grid current THD to 2.41%. The ANN controller accurately estimates the required compensating current and provides faster dynamic response, resulting in better suppression of lower- and higher-order harmonic components. Consequently, the grid current becomes more sinusoidal with improved waveform quality and reduced distortion.

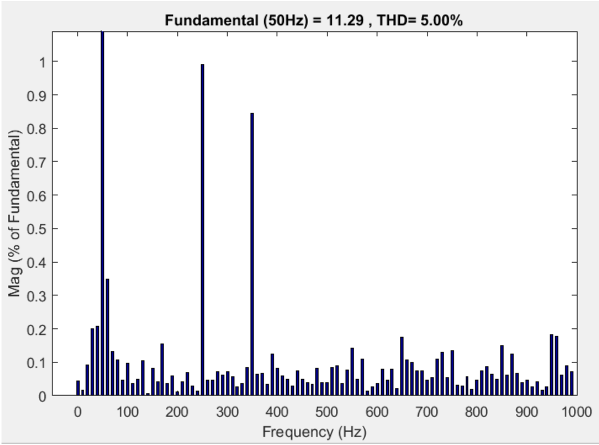

(a)

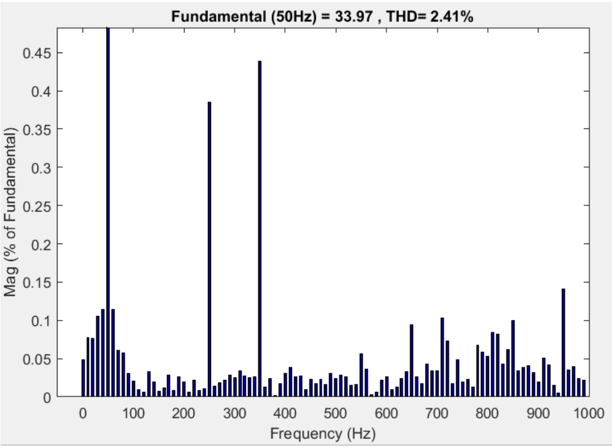

(b)

Fig. 15. Harmonic spectrum of the grid current: (a) PI controller (b) proposed ANN controller.

X. CONCLUSION

This paper presented a grid-connected solar photovoltaic (PV) and battery energy storage system integrated with a Dynamic Voltage Restorer (DVR) and a Shunt Active Power Filter (SAPF) for simultaneous power quality improvement and system stability enhancement. The proposed system employs a DC–DC boost converter with P&O maximum power point tracking (MPPT) to maximize solar energy extraction, while a bidirectional DC–DC converter enables efficient battery charging and discharging. An Artificial Neural Network (ANN) controller was developed to regulate the DC-link voltage and improve the dynamic response of the SAPF. In addition, the DVR effectively mitigated voltage sag and voltage swell by injecting the required series compensating voltage, thereby maintaining a regulated load voltage under grid disturbances. The SAPF successfully compensated harmonic currents, improved the source current waveform, and provided reactive power support. Simulation results obtained using MATLAB/Simulink demonstrated stable DC-link voltage regulation, reliable power sharing between the PV array and battery, effective voltage compensation, and significant harmonic reduction. Furthermore, the proposed ANN-based controller reduced the grid current THD from 5.00% to 2.41%, satisfying the IEEE-519 harmonic standard. Therefore, the proposed control strategy offers an efficient, reliable, and intelligent solution for enhancing power quality and system stability in renewable energy integrated smart grid applications.

Conflict of interest statement

Authors declare that they do not have any conflict of interest.

REFERENCES

[1] X. Liang, "Emerging power quality challenges due to integration of renewable energy sources," IEEE Trans. Ind. Appl., vol. 53, no. 2, pp. 855–866, Mar. 2017.

[2] A. Gupta, S. Doolla, and K. Chatterjee, "Hybrid AC–DC microgrid: Systematic evaluation of control strategies," IEEE Trans. Smart Grid, vol. 9, no. 4, pp. 3830–3843, Jul. 2018.

[3] S. Alshahrani, M. Khalid, and M. Almuhaini, "Electric vehicles beyond energy storage and modern power networks: Challenges and applications," IEEE Access, vol. 7, pp. 99031–99064, 2019.

[4] T. V. Thang, A. Ahmed, C.-I. Kim, and J.-H. Park, "Flexible system architecture of stand-alone PV power generation with energy storage device," IEEE Trans. Energy Convers., vol. 30, no. 4, pp. 1386–1396, Dec. 2015.

[5] J. von Appen, M. Braun, T. Stetz, K. Diwold, and D. Geibel, "Time in the sun: The challenge of high PV penetration in the German electric grid," IEEE Power Energy Mag., vol. 11, no. 2, pp. 55–64, Mar. 2013.

[6] S. K. Chaudhary, J. M. Guerrero, and R. Teodorescu, "Enhancing the capacity of the AC distribution system using DC interlinks—A step toward future DC grid," IEEE Trans. Smart Grid, vol. 6, no. 4, pp. 1722–1729, Jul. 2015.

[7] Liu, H. Li, X. Zhang, G. Feng, and Z. Du, "V2G integration based on a UPQC with SMES," IEEE Trans. Appl. Supercond., vol. 34, no. 8, pp. 1–3, Nov. 2024.

[8] D. I. Brandao, R. P. D. Santos, W. W. A. G. Silva, T. R. Oliveira, and P. F. Donoso-Garcia, "Model-free energy management system for hybrid alternating current/direct current microgrids," IEEE Trans. Ind. Electron., vol. 68, no. 5, pp. 3982–3991, May 2021.

[9] R. Zhu, M. Liserre, M. Langwasser, and C. Kumar, "Operation and control of the smart transformer in meshed and hybrid grids: Choosing the appropriate smart transformer control and operation scheme," IEEE Ind. Electron. Mag., vol. 15, no. 1, pp. 43–57, Mar. 2021.

[10] R. R. A. Nunez, J. Posada, C. Unsihuay-Vila, and O. Pinzon-Ardila, "Review of smart transformer-based meshed hybrid microgrids: Shaping, topology and energy management systems," IEEE Access, vol. 11, pp. 130165–130185, 2023.

[11] V. Jain and B. Singh, "Power quality improvement in PV system tied to weak grid," IEEE Trans. Ind. Appl., vol. 57, no. 2, pp. 1265–1273, Mar. 2021.

[12] P. Shukl and B. Singh, "Recursive digital filter based control for power quality improvement of grid tied solar PV system," IEEE Trans. Ind. Appl., vol. 56, no. 4, pp. 3412–3421, Jul. 2020.

[13] S. K. Dash and P. K. Ray, "A new PV-open-UPQC configuration for voltage sensitive loads utilizing novel adaptive controllers," IEEE Trans. Ind. Informat., vol. 17, no. 1, pp. 421–429, Jan. 2021.

[14] M. A. Mansor, K. Hasan, M. M. Othman, S. Z. B. M. Noor, and I. Musirin, "Construction and performance investigation of three-phase solar PV and battery energy storage system integrated UPQC," IEEE Access, vol. 8, pp. 103511–103538, 2020.

[15] C. Kumar, M. K. Mishra, and S. Mekhilef, “A new voltage control strategy to improve performance of DSTATCOM in electric grid,” CES Trans. Electr. Mach. Syst., vol. 4, no. 4, pp. 295–302, Dec. 2020.

[16] C. Kumar and M. K. Mishra, “Predictive voltage control of transformerless dynamic voltage restorer,” IEEE Trans. Ind. Electron., vol. 62, no. 5, pp. 2693–2697, May 2015.

[17] S. Devassy and B. Singh, “Design and performance analysis of threephase solar PV integrated UPQC,” IEEE Trans. Ind. Appl., vol. 54, no. 1, pp. 73–81, Jan. 2018.

[18] P. Ray, P. K. Ray, and S. K. Dash, “Power quality enhancement and power flow analysis of a PV integrated UPQC system in a distribution network,” IEEE Trans. Ind. Appl., vol. 58, no. 1, pp. 201–211, Jan. 2022.

[19] C. D. Sanjenbam, B. Singh, and P. Shah, “Reduced voltage sensors based UPQC tied solar PV system enabling power quality improvement,” IEEE Trans. Energy Convers., vol. 38, no. 1, pp. 392–403, Mar. 2023.

[20] S. Devassy and B. Singh, “Performance analysis of solar PV array and battery integrated unified power quality conditioner for microgrid systems,” IEEE Trans. Ind. Electron., vol. 68, no. 5, pp. 4027–4035, May 2021.

[21] V. M. Hrishikesan, D. Kumar, D. Das, and C. Kumar, “Operation and control of unified power quality conditioner enabled meshed hybrid microgrid,” in Proc. IEEE 15th Int. Conf. Compat., Power Electron. Power Eng. (CPE-POWERENG), Jul. 2021, pp. 1–6.

[22] A. Ghosh and G. Ledwich, Power Quality Enhancement Using Custom Power Devices. Cham, Switzerland: Springer, 2012.

[23] J. Rocabert, A. Luna, F. Blaabjerg, and P. Rodriguez, “Control of power converters in AC microgrids,” IEEE Trans. Power Electron., vol. 27, no. 11, pp. 4734–4749, Nov. 2012.

[24] H. Markiewicz and A. Klajn, “Standard EN 50160-voltage characteristics in public distribution systems,” Wroclaw, Poland, Wroclaw Univ. Technol., Tech. Rep. Jul. 2004.

[25] S. K. Yadav, A. Patel, and H. D. Mathur, “Study on comparison of power losses between UPQC and UPQC-DG,” IEEE Trans. Ind. Appl., vol. 58, no. 6, pp. 7384–739